

Artificial photosynthetic system for diluted CO₂ reduction in gas-solid phase

Received: 1 May 2024

Accepted: 26 September 2024

Published online: 11 October 2024



Ya Wang^{1,3}, Jian-Xin Wei^{1,3}, Hong-Liang Tang¹, Lu-Hua Shao¹,
Long-Zhang Dong^{1,2}, Xiao-Yu Chu¹, Yan-Xia Jiang¹, Gui-Ling Zhang¹,
Feng-Ming Zhang¹✉ & Ya-Qian Lan²✉

Rational design of robust photocatalytic systems to direct capture and in-situ convert diluted CO₂ from flue gas is a promising but challenging way to achieve carbon neutrality. Here, we report a new type of host-guest photocatalysts by integrating CO₂-enriching ionic liquids and photoactive metal-organic frameworks PCN-250-Fe₂M (M = Fe, Co, Ni, Zn, Mn) for artificial photosynthetic diluted CO₂ reduction in gas-solid phase. As a result, [Emim]BF₄(39.3 wt%)@PCN-250-Fe₂Co exhibits a record high CO₂-to-CO reduction rate of 313.34 μmol g⁻¹ h⁻¹ under pure CO₂ atmosphere and 153.42 μmol g⁻¹ h⁻¹ under diluted CO₂ (15%) with about 100% selectivity. In scaled-up experiments with 1.0 g catalyst and natural sunlight irradiation, the concentration of pure and diluted CO₂ (15%) could be significantly decreased to below 85% and 10%, respectively, indicating its industrial application potential. Further experiments and theoretical calculations reveal that ionic liquids not only benefit CO₂ enrichment, but also form synergistic effect with Co²⁺ sites in PCN-250-Fe₂Co, resulting in a significant reduction in Gibbs energy barrier during the rate-determining step of CO₂-to-CO conversion.

Direct capture and in situ conversion of diluted CO₂ from flue gas into value-added chemical stocks and fuels driven by natural abundant solar energy is a promising strategy to mitigate the superfluous greenhouse gas and achieve the utilization of CO₂^{1–4}. The prominent merit of this strategy lies in bypassing the energy-intensive processes of CO₂ separation and enrichment in conventional CO₂ utilization technology^{5,6}. In fact, the contained H₂O vapor (8–12 wt%) in common flue gas could serve as sacrificial agent in CO₂ reduction reaction, and gas-solid artificial photosynthesis overall reaction of CO₂ reduction is feasible, which is more appropriate for practical industrial application^{7–9}. In recent years, various semiconductor photocatalysts with high activity and selectivity have been developed for artificial photosynthetic CO₂ reduction to target products under a pure CO₂ atmosphere^{10–15}. Although many photocatalysts have exhibited high reduction activity in a pure CO₂ atmosphere, their artificial photosynthetic activity usually turned into extremely low level under diluted

CO₂ condition^{16–18}. One of the primary reasons for this is attributed to the sluggish CO₂ adsorption process which hinders the overall reaction kinetics^{18–20}. Because the anthropogenic CO₂ concentration derived from industrial gaseous waste (~15% CO₂) is relatively low^{21–23}. It is of great significance to develop robust artificial photosynthetic systems that can effectively enrich diluted CO₂ and simultaneously realize in situ reduction^{24–26}.

Metal-organic frameworks (MOFs), as a type of crystalline porous materials composed of organic ligands and metal nodes, have shown great potential in the field of artificial photosynthesis due to their intrinsic advantages, such as high surface area, structural tunability, customizable light absorption, and abundant open metal sites^{27–31}. In addition, the porous nature of MOFs also provides great opportunities of loading guest species to endow the materials with the aimed function by post synthetic modification^{32,33}. Generally, the organic ligands of MOFs serve as light absorber while the metal clusters act as

¹Heilongjiang Provincial Key Laboratory of CO₂ Resource Utilization and Energy Catalytic Materials, School of Material Science and Chemical Engineering, Harbin University of Science and Technology, Harbin, Heilongjiang 150080, China. ²School of Chemistry, South China Normal University, Guangzhou 510006, China. ³These authors contributed equally: Ya Wang, Jian-Xin Wei. ✉ e-mail: zhangfm80@163.com; yqlan@njnu.edu.cn

reduction and/or oxidation sites in artificial photosynthetic reactions^{34–36}. For example, a pyrazolyl porphyrinic Ni-MOF (PCN-601) realized visible-light-driven overall CO₂ reduction with H₂O vapor at room temperature, with the porphyrin ligand serving as a light harvester and generating electron-hole pairs³⁷. Previously, our group firstly proved that heterometallic nodes in MOFs could serve as CO₂ reduction and H₂O oxidation centers separately by using Fe₂M-based NNU-31-M (M = Ni, Co, Zn) as artificial photosynthetic overall reaction catalysts³⁸. Despite significant progress has been achieved in MOF artificial photosynthetic systems, the attempts to utilize MOF-based photocatalysts for the reduction of diluted CO₂ often result in extremely low activity, which is far from practical application^{39–41}. Ionic liquids (ILs) are an excellent type of CO₂ absorption materials with high ionic conductivity, low volatility, and high thermal stability merits^{42–44}. By using the CO₂ absorption ability of ILs, researchers have successfully constructed ILs@MOFs materials to enhance CO₂ adsorption and achieve diluted CO₂ enrichment^{45,46}. Based on the above, we reasoned that the combination of CO₂-enriching ILs and photoactive MOFs has great potential to achieve efficient low-concentration CO₂ reduction. Nevertheless, it is still a blank about combining the advantages of ILs and MOFs for artificial photosynthetic overall reaction, especially for diluted CO₂ reduction.

In this work, a series of heterometallic MOFs, PCN-250-Fe₂M (M = Fe, Co, Ni, Zn, Mn) with visible-light-harvesting azo-based ligands, were chosen as host photocatalysts, and typical imidazole-based ILs with excellent CO₂ enriching ability as guest species were introduced into the pores to construct host-guest photocatalysts for diluted CO₂ reduction in gas-solid reaction (Fig. 1). It was confirmed that the [Emim]BF₄(39.3 wt%)@PCN-250-Fe₂Co ([Emim]BF₄: 1-ethyl-3-

methylimidazole tetrafluoroborate) exhibits about 1.88 times higher CO₂ absorption amount than pure PCN-250-Fe₂Co. Without the addition of any photosensitizers and sacrificial agents, [Emim]BF₄@PCN-250-Fe₂Co shows an optimal CO₂-to-CO conversion rate of 313.34 μmol g⁻¹ h⁻¹, which is about 25 times higher than that of pristine PCN-250-Fe₂Co (12.27 μmol g⁻¹ h⁻¹). Notably, the host-guest photocatalyst reaches a record high photocatalytic activity of 153.42 μmol g⁻¹ h⁻¹ under diluted CO₂ (15%) atmosphere. The CO₂ concentration (15%) could be apparently decreased to below 10% in the scaled-up experiment with 1.0 g catalysts in 1072 cm² reactor under natural sunlight irradiation, showing its practical application potential. Further experimental and theoretical results suggest that the loaded ILs can effectively enrich diluted CO₂, and simultaneously transfer the activated CO₂ to Co²⁺ sites. The Gibbs free energy barrier in the rate-determining step of *COOH-Emim formation is significantly reduced by host-guest synergistic effect between ILs and Co²⁺ sites in PCN-250-Fe₂Co, leading to an overall improvement in the activity of artificial photosynthetic diluted CO₂ reduction.

Results

Synthesis and structural characterization of ILs@MOFs

PCN-250-Fe₂Co was synthesized via a solvothermal reaction between preformed Fe₂Co clusters and 3,3',5,5'-azo-benzene tetra-carboxylic acid (H₄abtc) ligand in the presence of acetic acid as a competing reagent⁴⁷. Subsequently, a representative ionic liquid [Emim]BF₄ with high CO₂ absorption capacity was introduced into the pores of PCN-250-Fe₂Co to prepare [Emim]BF₄@PCN-250-Fe₂M composites, as shown in Fig. 2a. The powder X-ray diffraction (PXRD) pattern of the synthesized PCN-250-Fe₂Co in Fig. 2b agrees well with the simulated

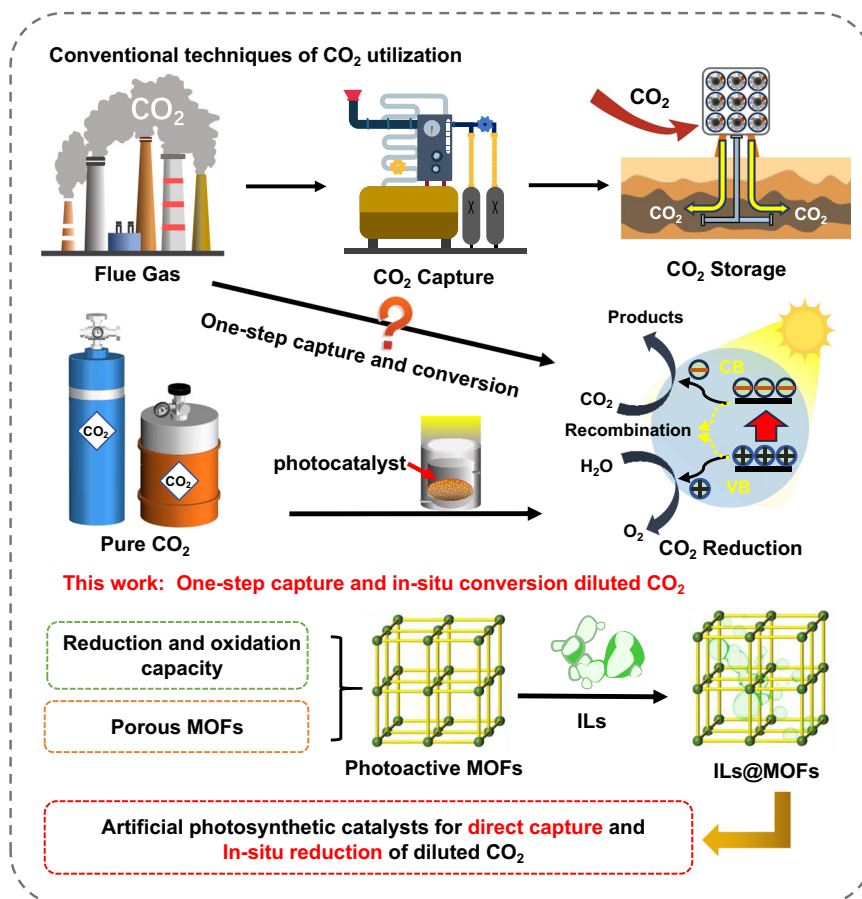


Fig. 1 | Schematic representation of conventional techniques of CO₂ utilization from flue gas and our new strategy for the construction of host-guest photocatalysts to direct capture and in situ reduction of diluted CO₂. ILs ionic liquids, MOFs metal-organic frameworks.

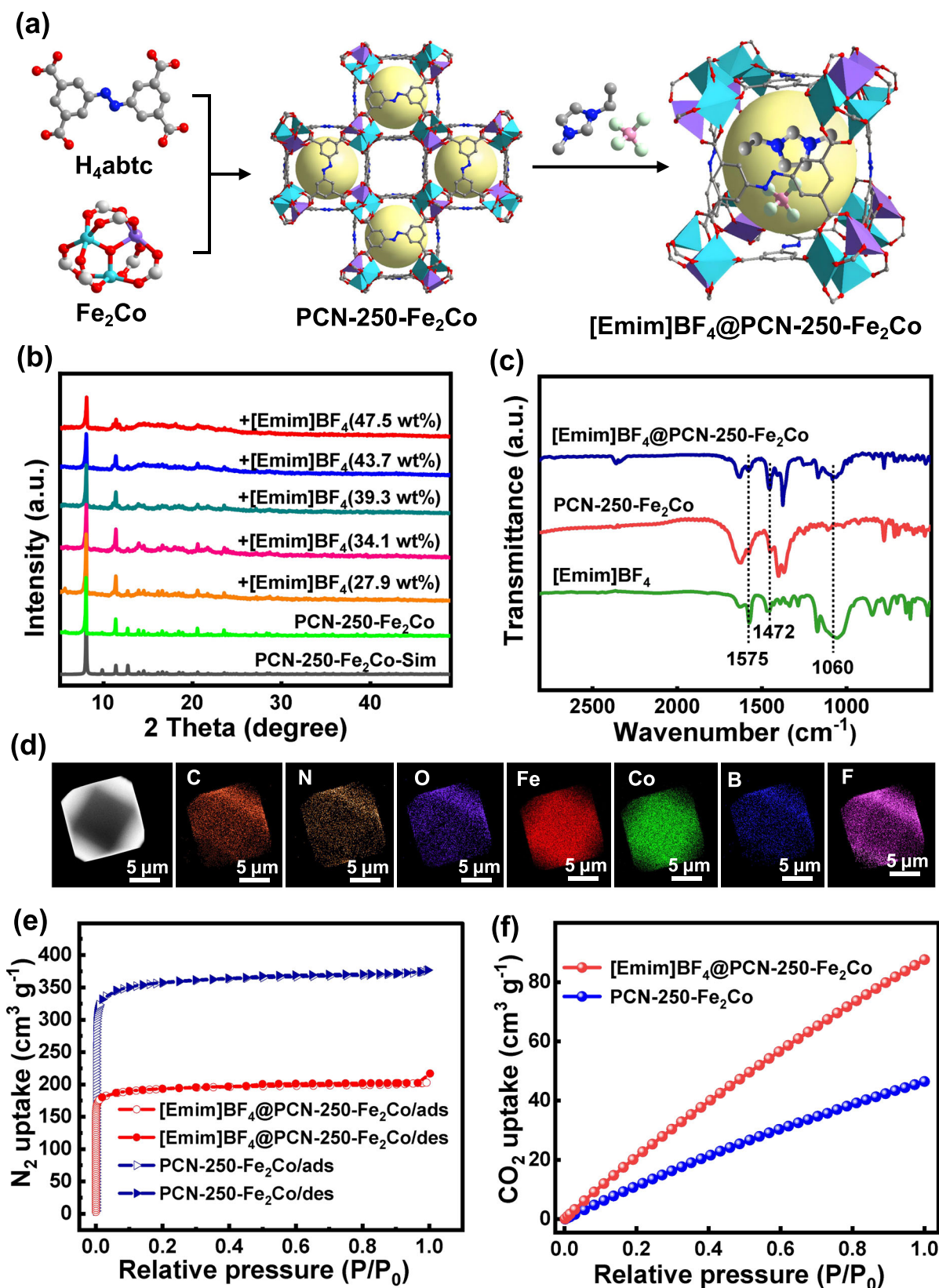


Fig. 2 | Synthetic procedures and characterizations of $[\text{Emim}]\text{BF}_4@PCN-250-\text{Fe}_2\text{M}$. **a** Synthesis of $[\text{Emim}]\text{BF}_4@PCN-250-\text{Fe}_2\text{M}$. H_4abtc : 3,3',5,5'-azobenzene tetra-carboxylic acid, Fe_2Co : $\text{Fe}_2\text{Co}(\mu_3\text{-O})(\text{CH}_3\text{COO})_6$, $[\text{Emim}]\text{BF}_4$: 1-ethyl-3-methylimidazolium tetrafluoroborate. **b** PXRD patterns of $PCN-250-\text{Fe}_2\text{Co}$ and $[\text{Emim}]\text{BF}_4@PCN-250-\text{Fe}_2\text{Co}$. **c** FT-IR spectra of $PCN-250-\text{Fe}_2\text{Co}$, $[\text{Emim}]\text{BF}_4$ and

$[\text{Emim}]\text{BF}_4(39.3 \text{ wt\%})@PCN-250-\text{Fe}_2\text{Co}$. **d** TEM images and EDS elemental mapping of $[\text{Emim}]\text{BF}_4(39.3 \text{ wt\%})@PCN-250-\text{Fe}_2\text{Co}$. **e** N_2 adsorption-desorption isotherms (77 K) and **f** CO_2 adsorption of $PCN-250-\text{Fe}_2\text{Co}$ and $[\text{Emim}]\text{BF}_4(39.3 \text{ wt\%})@PCN-250-\text{Fe}_2\text{Co}$. Source data are provided as a Source data file.

pattern, demonstrating the successful synthesis of PCN-250-Fe₂Co. The scanning electron microscopy (SEM) images reveal that PCN-250-Fe₂Co exhibits polyhedral shape with a particle size of ~10 μm (Supplementary Fig. 1). The transmission electron microscopy (TEM) images and energy dispersive X-ray spectroscopy (EDS) elemental mappings of PCN-250-Fe₂Co indicate that the Fe and Co elements are evenly distributed over the whole material and the atomic ratio of Fe/Co is of approximate 2:1, in agreement with the theoretical value (Supplementary Figs. 2 and 3, Supplementary Table 1). Furthermore, the X-ray photoelectron spectroscopy (XPS) spectra support the heterometallic nature of PCN-250-Fe₂Co (Supplementary Figs. 4 and 5)⁴⁸.

The Fourier transform infrared (FT-IR) and XPS spectroscopy have been applied to study the chemical compositions of [Emim]BF₄@PCN-250-Fe₂Co. The FT-IR spectrum of [Emim]BF₄@PCN-250-Fe₂Co displays a peak around 1060 cm⁻¹, which corresponds to the stretching vibration peak of B-F bond^{49,50}. In addition, the peaks at 1472 and 1575 cm⁻¹ can be ascribed to the stretching vibration of C=C and C=N bonds on the imidazole ring, respectively (Fig. 2c)^{51–53}. The XPS spectrum of F 1s shows a strong peak at 685.82 eV, which is attributed to the negatively charged BF₄⁻, indicating the successful integration of [Emim]BF₄ and PCN-250-Fe₂Co (Supplementary Fig. 6). After [Emim]BF₄ loading, the crystalline structure of PCN-250-Fe₂Co retained (Fig. 2b), and its morphology of [Emim]BF₄@PCN-250-Fe₂Co was consistent with the parent PCN-250-Fe₂Co, with a uniform distribution of F and B elements (Fig. 2d and Supplementary Fig. 7). The thermogravimetric analysis (TGA) conducted under air atmosphere reveals that both PCN-250-Fe₂Co and [Emim]BF₄@PCN-250-Fe₂Co could remain their structural integration up to 350 °C (Supplementary Fig. 8).

As confirmed by N₂ adsorption and desorption measurements at 77 K (Fig. 2e), both PCN-250-Fe₂Co and [Emim]BF₄@PCN-250-Fe₂Co exhibit type-I absorption characteristics with a rapid N₂ uptake at low relative pressure. The introduction of [Emim]BF₄ into the pores of PCN-250-Fe₂Co led to a decrease in Brunauer-Emmett-Teller (BET) surface area from 960.8 to 482.6 m² g⁻¹. Furthermore, the pore size decreased from 0.82 nm to 0.48 nm (Supplementary Fig. 9), indicating that the pore channel space of PCN-250-Fe₂Co was occupied by [Emim]BF₄. Although the BET surface area and pore size of PCN-250-Fe₂Co obviously decreased after loading [Emim]BF₄, its CO₂ adsorption capability increased significantly with the addition amount of ILs (Supplementary Fig. 10). As shown in Fig. 2f, [Emim]BF₄(39.3 wt%)/PCN-250-Fe₂Co exhibits a CO₂ adsorption capacity of 87.3 cm³ g⁻¹ at 298 K, which is ~1.88 times higher than that of PCN-250-Fe₂Co (46.4 cm³ g⁻¹). The enhanced CO₂ enrichment ability of [Emim]BF₄@PCN-250-Fe₂Co lays a solid foundation for high photocatalytic activity.

The optical absorption property and band gap of PCN-250-Fe₂Co were investigated by UV–vis diffuse reflectance spectroscopy (DRS). PCN-250-Fe₂Co exhibited considerable absorption in the UV and visible regions (Supplementary Fig. 11), and the band gap of PCN-250-Fe₂Co is estimated to be 1.85 eV from Tauc plots (Supplementary Fig. 12). According to Mott-Schottky measurements (Supplementary Fig. 13), the flat band potential of PCN-250-Fe₂Co is -0.66 V referenced to the Ag/AgCl electrode. Considering the conduction band (CB) position of n-type semiconductor is generally 0.1 V more negative than the flat band potential⁵⁴, the CB position of PCN-250-Fe₂Co is derived to be -0.56 V vs. normal hydrogen electrode (NHE). Meanwhile, the valence band (VB) position is calculated to be 1.29 V through band gap and the CB value. It is obvious that the CB value of PCN-250-Fe₂Co is more negative than the standard potential of CO₂ reduction to CO (-0.52 V vs. NHE at pH = 7), and the VB value is more positive than the standard potential of H₂O oxidation to O₂ (0.82 V vs. NHE at pH = 7), indicating its abilities to achieve the overall reactions of CO₂ reduction and H₂O oxidation (Supplementary Fig. 14).

Study of photocatalytic CO₂ conversion

The photocatalytic CO₂ reduction performances of [Emim]BF₄@PCN-250-Fe₂Co were evaluated in gas–solid reaction under visible light irradiation (300 W Xe lamp with a cut-off filter of 420 nm) without adding any photosensitizers, sacrificial agents or promoters. The as-synthesized [Emim]BF₄@PCN-250-Fe₂Co composites were uniformly coated on a glass before photocatalytic tests. As shown in Fig. 3a and Supplementary Fig. 15, a series of [Emim]BF₄@PCN-250-Fe₂Co with different loading amounts of [Emim]BF₄ exhibited significantly improved CO₂-to-CO reduction activity compared to that of parent PCN-250-Fe₂Co. An optimal photocatalytic CO evolution rate of 313.34 μmol g⁻¹ h⁻¹ was observed when the loading amount of [Emim]BF₄ reached 39.3 wt%, which is ~25 times higher than the activity of pristine PCN-250-Fe₂Co (12.27 μmol g⁻¹ h⁻¹). In addition, the detected CO/O₂ production amounts are close to the stoichiometric ratio of 2:1 (Supplementary Fig. 16), indicating it is an artificial photosynthetic overall reaction of CO₂ reduction and H₂O oxidation. It is noteworthy that the CO₂ reduction activity of [Emim]BF₄(39.3 wt%)/PCN-250-Fe₂Co surpasses various reported photocatalysts under similar reaction condition (Supplementary Table 2). An apparent quantum efficiency (AQE) of 2.9% was obtained at 420 nm, and the change of AQE at diverse light irradiation wavelength was consistent with the tendency of light absorption curve (Supplementary Fig. 17). In addition, it is found that the optimal loading amount of [Emim]BF₄(39.3 wt%) for photocatalytic activity is comparable to the pore volume of PCN-250-Fe₂Co, which may ensure the loaded [Emim]BF₄ existing in the pores of MOF maximally. In control experiment, the sample obtained by simply mixing [Emim]BF₄ and PCN-250-Fe₂Co (denoted as IL + MOF) only exhibited a little improvement of CO production rate compared to pure MOF (Supplementary Fig. 18), demonstrating the necessity of loading ILs into the pores of MOFs for the enhanced photocatalytic activity in the system.

To evaluate the effect of different divalent metal species in Fe₂M cluster of MOFs on the photocatalytic activity, a series of PCN-250-Fe₂M (M = Mn, Zn, Ni, Fe) were synthesized (Supplementary Fig. 19). As confirmed, all PCN-250-Fe₂M possess suitable band energy positions for artificial photosynthetic CO₂ reduction overall reaction (Supplementary Figs. 12, 14, 20–23). Photocatalytic experiments confirmed that both PCN-250-Fe₂Co and [Emim]BF₄@PCN-250-Fe₂Co exhibited superior photocatalytic CO₂-to-CO conversion activities in comparison with other pure MOFs and composite systems, respectively (Fig. 3b). The influence of different ILs on the photocatalytic performance was further determined. Two other ILs, [Emim]Br (39.3 wt%) and [Emim]Ac (39.3 wt%), were selected and loaded into PCN-250-Fe₂Co to evaluate the photocatalytic properties. As shown in Fig. 3c, the combination of [Emim]BF₄ and PCN-250-Fe₂Co lead to the highest photocatalytic activity than others, which may be attributed to its high CO₂ adsorption capacity (Supplementary Fig. 24).

Encouraged by the excellent photocatalytic activity in pure CO₂ atmosphere, diluted CO₂ (15% CO₂ and 85% N₂) reduction activity of [Emim]BF₄@PCN-250-Fe₂Co was further studied. Under visible light irradiation, [Emim]BF₄@PCN-250-Fe₂Co still showed a high CO evolution rate of 153.42 μmol g⁻¹ h⁻¹ in gas–solid reaction with diluted CO₂ as source, while almost no CO can be detected for the pristine PCN-250-Fe₂Co under the same conditions (Fig. 3d). Thus, the remarkable photocatalytic activity of [Emim]BF₄@PCN-250-Fe₂Co under diluted CO₂ atmosphere should be attributed to the contribution of ILs which effectively enriched diluted CO₂. Notably, the host-guest [Emim]BF₄@PCN-250-Fe₂Co catalyst presents the most outstanding artificial photosynthetic CO evolution rate both in high and diluted CO₂ atmosphere (Fig. 3e, Supplementary Tables 2 and 3). It can be observed that only CO can be detected in the gas chromatography FID detector, while only O₂ can be detected in the gas chromatography TCD detector (Supplementary Fig. 25). Ion chromatography and ¹H NMR spectrum analyses confirmed no liquid products was produced in

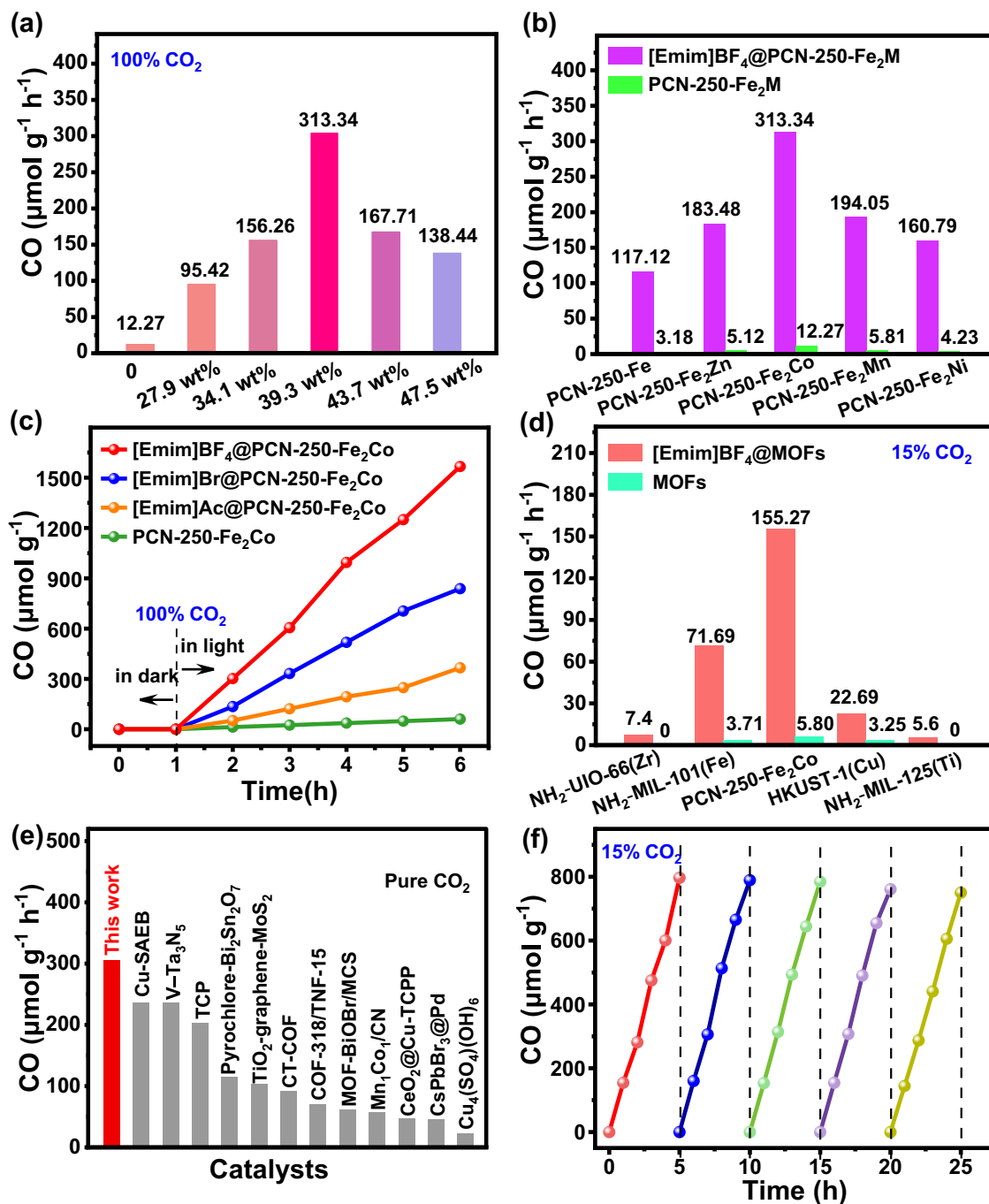


Fig. 3 | Photocatalytic conversion of CO₂ to CO. **a** Photocatalytic performance of PCN-250-Fe₂Co with different loading amounts of [Emim]BF₄. **b** Photocatalytic performance of PCN-250-Fe₂M and [Emim]BF₄@PCN-250-Fe₂M (M = Co, Mn, Zn, Ni, Fe). **c** Photocatalytic performance of PCN-250-Fe₂Co with different kinds of ILs. [Emim]Ac: 1-ethyl-3-methylimidazolium acetate, [Emim]Br: 1-ethyl-3-

methylimidazole bromide. **d** Photocatalytic performance of CO₂ reduction to CO under diluted CO₂ (15% CO₂ and 85% N₂) atmosphere. **e** Summary of photocatalytic CO₂ reduction activity under pure CO₂ atmosphere. **f** Photocatalytic stability of [Emim]BF₄(39.3 wt%)@PCN-250-Fe₂Co under diluted CO₂ atmosphere. Source data are provided as a Source data file.

photocatalytic reaction, indicating the CO production selectivity of ~100% (Supplementary Figs. 26 and 27). In addition, [Emim]BF₄@PCN-250-Fe₂Co exhibited consistent CO yielding rate during consecutive five cycles photocatalytic tests in both pure CO₂ and diluted CO₂ conditions (Fig. 3f and Supplementary Fig. 28). Meanwhile, the XRD patterns and SEM images reveal that the crystalline structure and morphology of [Emim]BF₄@PCN-250-Fe₂Co remain unchanged after five consecutive photocatalytic cycles (Supplementary Figs. 29–32), proving its stable photocatalytic performance.

The universality of the strategy in improving diluted CO₂ reduction by the integration of photocatalytic MOFs and CO₂-enriching ILs was further examined. Some typical MOFs with visible light absorption properties and high moisture stability were synthesized, then loading [Emim]BF₄ to prepare [Emim]BF₄@MOFs (Supplementary Fig. 33). As a result, all [Emim]BF₄@MOFs photocatalyst show apparently improved CO₂-to-CO conversion activities in comparison with pristine MOFs both under pure and diluted CO₂ (Fig. 3d and Supplementary Figs. 34–37), suggesting the effectiveness of a host-guest

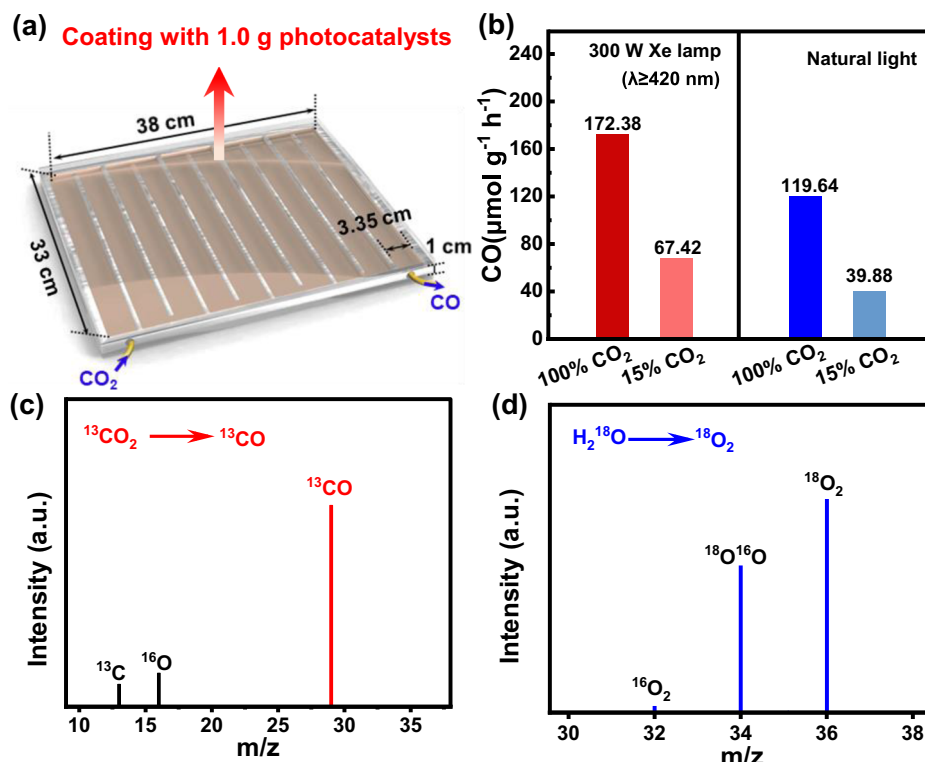


Fig. 4 | Scaled-up experiments and carbon/oxygen source origin determination. **a** Illustration of a photocatalytic experimental device for scaled-up experiments. **b** Photocatalytic performance of [Emim]BF₄@PCN-250-Fe₂Co in scaled-up

experiments. **c** Mass spectroscopy of ¹³CO (m/z = 29) produced from ¹³CO₂ reduction. **d** Mass spectroscopy of ¹⁸O₂ (m/z = 36) produced from H₂O oxidation. Source data are provided as a Source data file.

Table 1 | CO₂ concentration of [Emim]BF₄@PCN-250-Fe₂Co after scaled-up experiments

CO ₂ source	Light conditions	10 h	20 h	30 h	40 h	50 h	60 h
Pure CO ₂	300 W Xe lamp (λ ≥ 420 nm), ~390 mW/cm ²	94.88%	90.21%	85.94%	82.02%	78.39%	75.36%
	Natural light, ~100 mW/cm ²	96.90%	94.10%	91.48%	88.91%	86.52%	84.27%
15% CO ₂	300 W Xe lamp (λ ≥ 420 nm), ~390 mW/cm ²	12.79%	10.91%	9.32%	7.88%	6.55%	5.44%
	Natural light, ~100 mW/cm ²	13.53%	12.43%	11.58%	10.83%	10.26%	9.85%

Source data are provided as a Source data file.

photocatalytic system based on MOFs and ILs. Among all [Emim]BF₄@MOFs, [Emim]BF₄@PCN-250-Fe₂Co exhibits the best photocatalytic activity, which may be attributed to its intrinsic azo units in the ligands and heterometallic clusters with unsaturated metal centers, benefitting light absorption and the providing sufficient reduction and oxidation sites for overall photocatalytic reactions³⁸.

To explore the practical application potential of the host-guest photocatalyst, we made a scaled-up glass reactor with a surface area of 1072 cm² coating with 1.0 g photocatalyst and conducted the scaled-up test for 60 h (Fig. 4a and Supplementary Fig. 38). After the reaction under visible light and natural sunlight irradiation, the pure CO₂ concentration was observed to decrease to 75.36% and 84.27%, respectively, and the diluted CO₂ (15%) decreased to 5.44% and 9.85%, as detailed in Table 1. [Emim]BF₄@PCN-250-Fe₂Co achieved a visible-light-driven CO₂-to-CO conversion rate up to 172.38 μmol g⁻¹ h⁻¹ under pure CO₂ condition and 67.42 μmol g⁻¹ h⁻¹ under a diluted CO₂ atmosphere. Meanwhile, under natural sunlight irradiation at 298 K, the photocatalytic CO evolution rate still reached 119.64 and 39.88 μmol g⁻¹ h⁻¹ under pure and diluted CO₂ conditions, respectively (Fig. 4b and Supplementary Fig. 39). It is worth mentioning that gram-scale PCN-250-Fe₂Co (about 15.0 g) can be facile obtained in one day

by stirring/reflux method (Workflow see Supplementary Information and Supplementary Fig. 40), which lays a solid foundation for its extensive use. The above experimental results show the application perspective of ILs@MOFs host-guest photocatalysts in direct diluted CO₂ reduction. The isotope ¹³CO₂ tracing experiment was performed to determine the carbon source origin of CO product. As detected by gas chromatography-mass spectrometry (GC-MS), the reduction product ¹³CO (m/z = 29) was observed by using ¹³CO₂ as source (Fig. 4c). The oxygen source of oxidation product O₂ was also checked by isotopic labeling experiment, and ¹⁸O₂ (m/z = 36) and ¹⁸O¹⁶O (m/z = 34) were detected by GC-MS when using H₂¹⁸O as the reaction solvent (Fig. 4d). The above results confirm that the photocatalyst really drive overall reaction of CO₂ reduction and H₂O oxidation.

Mechanistic insights into the photocatalytic CO₂ reduction processes

The photoelectrochemical measurements for PCN-250-Fe₂Co and [Emim]BF₄@PCN-250-Fe₂Co were performed to investigate the effect of ILs loading on the separation and migration behavior of photo-generated electron-hole pairs. It is found that the transient photocurrent intensity of [Emim]BF₄@PCN-250-Fe₂Co is nearly 3 times

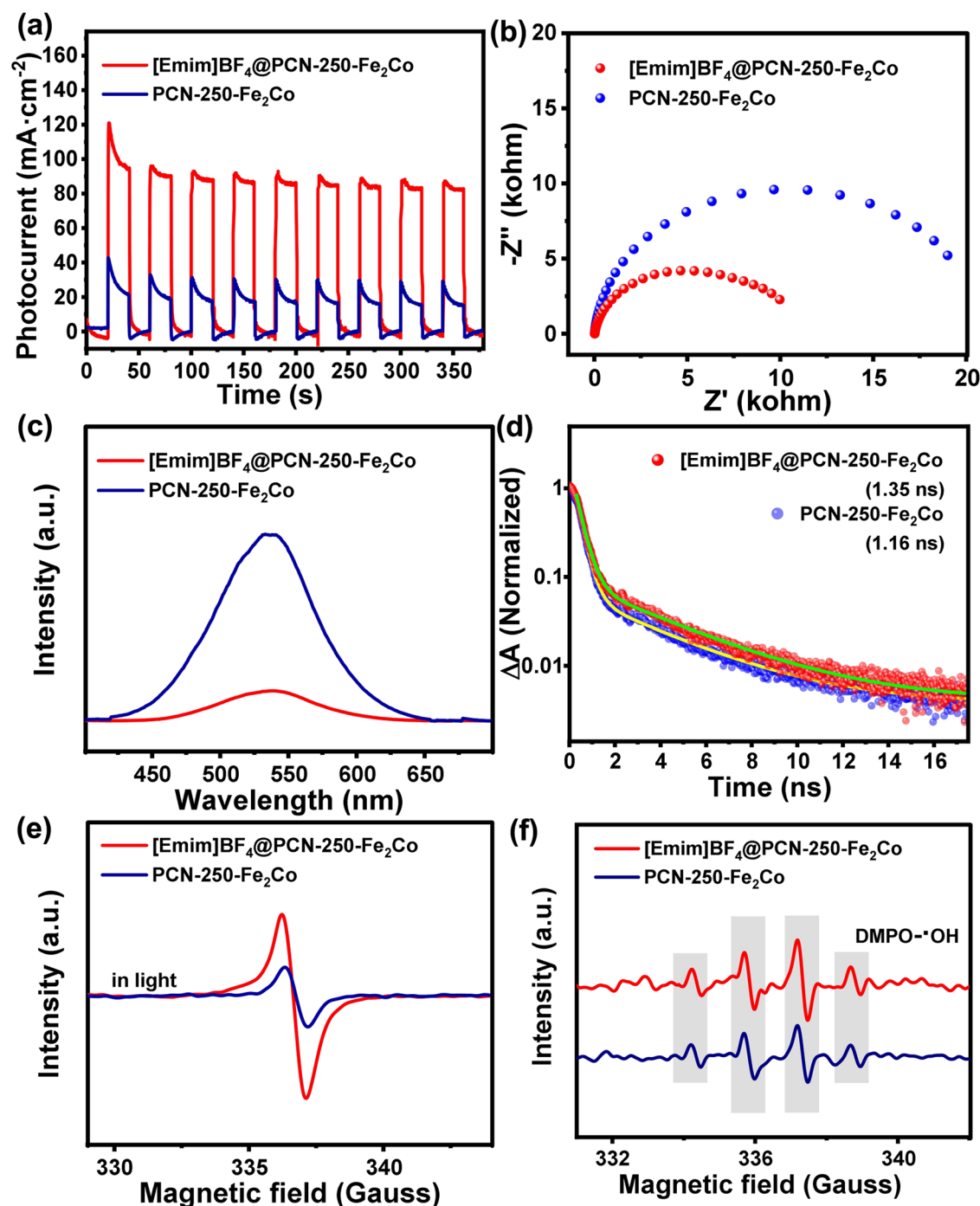


Fig. 5 | Comparisons for photochemical properties of PCN-250-Fe₂Co and [Emim]BF₄(39.3 wt%)/PCN-250-Fe₂Co. a Transient photocurrent responses. **b** EIS Nyquist plots. **c** Photoluminescence spectra. **d** Time-resolved PL spectra.

e EPR spectra with 420 nm light irradiation. **f** EPR spectra of •OH radical trapped by DMPO. Source data are provided as a Source data file.

higher than that of PCN-250-Fe₂Co (Fig. 5a). In addition, [Emim]BF₄@PCN-250-Fe₂Co possesses a smaller the radius of Nyquist curve compared to PCN-250-Fe₂Co (Fig. 5b). These indicate that more efficient charge transport existed in the composite. As shown in Fig. 5c, d, [Emim]BF₄@PCN-250-Fe₂Co exhibits weaker photoluminescence (PL) intensity and longer PL lifetimes than PCN-250-Fe₂Co, implying a lower recombination efficiency of photogenerated electrons and holes in [Emim]BF₄@PCN-250-Fe₂Co. The room-temperature electron paramagnetic resonance (EPR) spectra show that [Emim]BF₄@PCN-250-Fe₂Co owns a higher intensity of EPR signal upon light irradiation,

meaning that more free electrons could participate in photocatalytic reactions (Fig. 5e and Supplementary Figs. 41 and 42). The results of free radical trapping experiments indicate that the peaks intensity of DMPO-•OH (DMPO: 1,3-Dimethyl-5-pyrazolone) from [Emim]BF₄@PCN-250-Fe₂Co sample is apparently higher than that of PCN-250-Fe₂Co, suggesting its more potential for driving the oxidation reaction from H₂O to O₂ (Fig. 5f).

The in situ measurements combined with DFT calculations were conducted to further reveal the mechanism of the overall photocatalytic reaction (details in Supplementary Information). Using

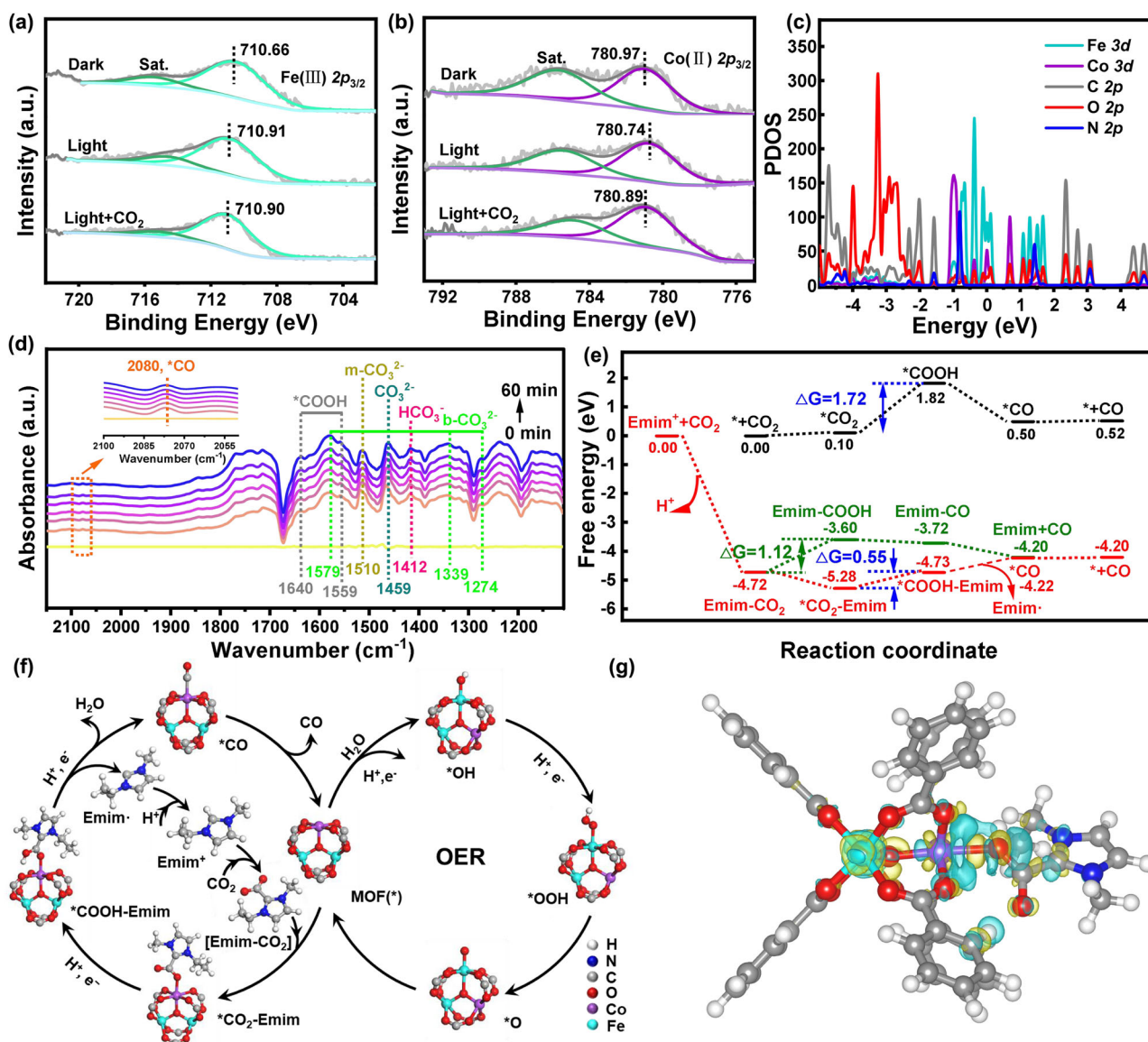


Fig. 6 | Mechanism for CO₂ photoreduction on [Emim]BF₄@PCN-250-Fe₂Co. In situ XPS spectra of **a** Fe 2p and **b** Co 2p for the simulated solar-driven CO₂ reduction process over PCN-250-Fe₂Co. **c** PDOS diagram of PCN-250-Fe₂Co. **d** In situ DRIFTS measurement of [Emim]BF₄@PCN-250-Fe₂Co for CO₂ reduction under visible light irradiation (irradiation time of 0, 10, 20, 30, 40, 50, 60 min, respectively). **e** Free energy profiles of PCN-250-Fe₂Co, Emim⁺ and [Emim]BF₄@PCN-250-Fe₂Co in the

process of photocatalytic CO₂ reduction to CO. **f** Schematic diagram of the photocatalytic CO₂ reduction and H₂O oxidation mechanism. **g** The differential charge density diagram of *CO₂-Emim. The yellow and blue contours represent charge accumulation and charge depletion, respectively. Source data are provided as a Source data file.

in situ XPS measurements can clearly reveal the electron transfer process in photochemical reactions of PCN-250-Fe₂Co. As shown in Fig. 6a, b, under light irradiation, the binding energy of Fe 2p in PCN-250-Fe₂Co increases from 710.66 to 710.91 eV. In contrast, the binding energy of Co 2p decreases from 780.97 to 780.74 eV, indicating that electrons transfer to the Co sites under photoexcitation. After introducing CO₂ into the system, the binding energy of Co 2p increases to 780.89 eV, and the binding energy of Fe 2p remains nearly unchanged, indicating that the photogenerated electrons transferred from Co²⁺ to CO₂. Moreover, the C 1s spectra exhibit a shift towards lower binding energy upon exposure to light in the presence of CO₂, which indicates the adsorbed CO₂ molecules receive electrons from the Co²⁺ (Supplementary Fig. 43). Consequently, it can be inferred that Co²⁺ serve as the active sites for the photocatalytic reduction of CO₂ to CO and Fe³⁺ for the H₂O oxidation to O₂⁵⁵. Combining with DFT calculations, the projected density of

states (PDOS) diagram was calculated based on optimized crystal geometry of PCN-250-Fe₂Co (Supplementary Fig. 44) to further confirm its active centers. As shown in Fig. 6c, it can be seen that the conduction band minimum (CBM) and the valence band maximum (VBM) are mainly contributed by the 3d orbitals of Co and the 3d orbitals of Fe, respectively. Therefore, photo-excited electrons and holes are mainly concentrated on Co²⁺ and Fe³⁺, suggestive of the active sites for CO₂ reduction and H₂O oxidation on PCN-250-Fe₂Co being Co²⁺ and Fe³⁺, respectively. In contrast, the 2p orbitals of N makes almost no contribution near the Fermi level, indicating that azo groups were not the main redox sites in the system. In addition, no CO product can be detected with individual [Emim]BF₄ as photocatalyst and even no photocatalytic improvement from [Emim]BF₄ can be observed in the system with [Ru(bpy)₃]Cl₂ as a photosensitizer and TEOA as a sacrificial agent (Supplementary Fig. 18), indicating the fact that IL itself can not serve as CO₂ reduction active site.

In situ diffuse reflectance infrared Fourier transform spectra (DRIFTS) was applied to detect the generated intermediates during the photocatalytic CO₂ reduction reaction in [Emim]BF₄@PCN-250-Fe₂Co, as shown in Fig. 6d. Upon CO₂ introduction in the dark, the characteristic peaks at 2335 and 2360 cm⁻¹ correspond to the gaseous and weakly adsorbed CO₂, which gradually raised over time with continued exposure to CO₂ (Supplementary Fig. 45a). Under illumination, these CO₂ characteristic peaks decreased over a period of 0 to 60 min, indicating the consumption and conversion of CO₂ (Supplementary Fig. 45b)⁵⁶. In contrast, the intensities of some new peaks gradually increased over illumination period. Notably, the peaks at 1274, 1339, and 1579 cm⁻¹ correspond to the bidentate carbonate (b-CO₃²⁻), while the peak at 1510 cm⁻¹ is attributed to the monodentate carbonate (m-CO₃²⁻)⁵⁵. The band at 1412 cm⁻¹ is assigned to the bicarbonate radical (HCO₃⁻)⁵⁵. The peak at 1459 cm⁻¹ matches the vibrational frequency of CO₃²⁻⁵⁷. The increased peaks of identified carboxylates suggests that [Emim]BF₄@PCN-250-Fe₂Co can chemically adsorb and interact with CO₂ and H₂O molecules. In addition, the peaks appearing at 1559 and 1640 cm⁻¹ after photoirradiation are ascribed to the formation of *COOH, which is a key intermediate during the photochemical conversion of CO₂ to CO¹⁴. In addition, the gradually enhanced peak at 2080 cm⁻¹ corresponds to the *CO intermediate, which is related directly to the formation of the final CO product³.

The electrostatic potential (ESP) analysis was employed to validate the host-guest interaction between the [Emim]BF₄ and PCN-250-Fe₂Co. From ESP map (Supplementary Fig. 46), it can be observed that there is a strong electrostatic interaction between [Emim]BF₄ and PCN-250-Fe₂Co. In order to clarify the contribution of ionic liquids on the CO₂ reduction performance, the Gibbs free energy of CO₂ adsorption process was firstly evaluated by DFT calculations to compare the CO₂ adsorption abilities of [Emim]BF₄, [Emim]Br, and [Emim]Ac. The spontaneous adsorption of CO₂ was observed on [Emim]BF₄ ($\Delta G = -0.02$ eV), whereas [Emim]Br and [Emim]Ac showed small energy barriers for CO₂ adsorption with ΔG values of 0.06 eV and 0.07 eV, respectively (Supplementary Table 4). These findings provide additional evidences to confirm the superior CO₂ adsorption abilities of [Emim]BF₄, which consistent with the experimental results. To further explore the CO₂ capture process of [Emim]BF₄, four possible adsorption mechanisms were considered (Supplementary Information). By comparing the change of Gibbs free energy for each adsorption process (Supplementary Fig. 47), the formation of Emim-CO₂ is highly favorable for CO₂ capture with lowest ΔG of -4.72 eV. Thus, in subsequent investigation of the photocatalytic mechanism, we focused on the crucial contribution of Emim⁺ in the host-guest synergistic effect.

As the free energy profiles in the CO₂-to-CO reaction pathway of PCN-250-Fe₂Co, Emim⁺ and [Emim]BF₄@PCN-250-Fe₂Co shown in Fig. 6e, f, the first step on Fe₂Co node is the adsorption of CO₂ molecule with the ΔG of 0.10 eV. For Emim⁺ and [Emim]BF₄@PCN-250-Fe₂Co, the Emim⁺ tends to spontaneously combine CO₂ molecules to form Emim-CO₂ and the adsorbed CO₂ molecules exhibit a bent structure (the bent angle $\angle O-C-O = 133.19^\circ$) (Supplementary Fig. 48), indicating the remarkable capability of [Emim]BF₄ in enriching and activating CO₂ molecule. To further investigate the CO₂ transfer process, we calculated the differential charge density of the crucial intermediate *CO₂-Emim. As illustrated in Fig. 6g, the electrons mainly concentrated on the area between Co²⁺ sites and CO₂ molecule absorbed on Emim, indicating that CO₂ molecule could be transferred from Emim-CO₂ to Co²⁺ active sites of PCN-250-Fe₂Co. Notably, the synergistic effect between Co²⁺ and Emim could effectively promote proton-coupled electron transfer process from *CO₂ to *COOH. As confirmed, the ΔG value of rate-determining step (RDS) for *COOH-Emim formation is 0.55 eV for [Emim]BF₄@PCN-250-Fe₂Co, which is much smaller than that of PCN-250-Fe₂Co (1.72 eV) and Emim⁺ (1.12 eV). Subsequently, Emim deviated from the *COOH-Emim intermediate and spontaneously bind with an H⁺ to form Emim⁺. On the other hand,

*COOH further get a photogenerated electron and proton pair to form CO with a minimal energy barrier (0.02 eV). Meanwhile, the RDS energy barrier of H₂O oxidation to form O₂ is lower on the Fe³⁺ site (1.91 eV) compared to the azo group (2.28 eV) (Supplementary Fig. 49). This further supports that Fe³⁺ is the active site for H₂O oxidation, finally completing the artificial photosynthetic overall reaction as shown in Fig. 6f. All the calculation results support that ILs plays a crucial role in facilitating artificial photosynthesis of diluted CO₂ and the host-guest synergistic mechanism of [Emim]BF₄@PCN-250-Fe₂Co is inferred.

Discussion

In summary, a host-guest synergistic artificial photosynthetic system was developed based on CO₂-enriching ILs and photoactive MOFs PCN-250 for direct capture and in situ reduction of diluted CO₂ in gas-solid phase. The [Emim]BF₄@PCN-250-Fe₂Co composite realized an impressive visible-light-driven CO₂-to-CO conversion rate of 313.34 $\mu\text{mol g}^{-1} \text{h}^{-1}$. Moreover, a record-breaking CO evolution rate of 153.42 $\mu\text{mol g}^{-1} \text{h}^{-1}$ was achieved under a diluted CO₂ (15%) atmosphere, surpassing all previously reported photocatalytic systems. In the scaled-up experiment under diluted CO₂ and natural light, the CO₂ concentration was decreased significantly below to 10% and a high CO yield of 39.88 $\mu\text{mol g}^{-1} \text{h}^{-1}$ was reached. Both experimental and theoretical calculated results indicate that the loaded [Emim]BF₄ serve as a CO₂ enrichment component, while the Co²⁺ and Fe³⁺ in PCN-250-Fe₂Co work as the active sites for CO₂ reduction and H₂O oxidation, respectively. Furthermore, the loaded ILs not only improve the adsorption capacity of CO₂, but also activate the adsorbed CO₂. The synergistic effect of the metal sites and ILs in [Emim]BF₄@PCN-250-Fe₂Co decreases the Gibbs free energy barrier for *COOH intermediate formation of CO product. This work reports a universal strategy for artificial photosynthetic diluted CO₂ conversion from flue gas and depth insights into the host-guest synergistic catalytic mechanism.

Methods

Material preparation

All of the reagents and solvents were commercially available and used without further purification.

Synthesis of PCN-250-Fe₂M. Fe₂M (Fe₂M(μ_3 -O)(CH₃COO)₆) metal clusters were synthesized according to the method reported in previous literature⁵⁸. A certain dose of crystalline sodium acetate (42 g, 0.31 mol) was dissolved in 70 mL water. And then ferric nitrate (8 g, 0.02 mol) was completely dissolved under magnetic stirring, then divalent metal nitrate was added. Stopping experiment after magnetic stirring for 1 h and left the liquid overnight. Then the membrane was removed and filtered under reduced pressure and washed with a large amount of ethanol at 100 °C after air drying for 24 h, the target metal cluster was obtained for reserve.

The PCN-250-Fe₂M materials were synthesized by solvothermal method according to the previous literature⁴⁷. The preformed Fe₂M clusters (0.015 g), 3,3',5,5'-azo-benzene tetra-carboxylic acid (H₄abtc) (0.01 g) and acetic acid (0.1 mL) were placed in 2 mL N,N-dimethyl formamide (DMF) and ultrasonic dissolved reagents into a Teflon-lined stainless-steel autoclave. The mixture was heated in an oven at 140 °C for 2 h. After reaction, the mixture was slowly cooled to room temperature. The dark brown precipitate formed by the reaction was filtered and washed with DMF for 3 times. The collected powder was soaked in anhydrous acetone for 48 h with the solvent changed for 5 times, and finally dried in vacuum at 120 °C for 12 h.

Gram-scale production of PCN-250-Fe₂Co. PCN-250-Fe₂Co were Gram-scale production by improving the synthetic method. The Fe₂Co clusters (1.5 g), 3,3',5,5'-azo-benzene tetra-carboxylic acid (H₄abtc) (1 g) and acetic acid (1 mL) were, respectively, placed in 200 mL N,N-

dimethyl formamide (DMF) and ultrasonic dissolved reagents into a 500 ml round bottom flask. The mixture was stirred and heated in a heating sleeve at 140 °C for 2 h. The dark brown precipitate formed by the reaction was filtered and washed with DMF for 3 times. After reaction, the mixture was slowly cooled to room temperature. The collected powder was soaked in anhydrous acetone for 48 h with the solvent changed for 5 times, and finally dried in vacuum at 120 °C for 12 h.

The calculation of material cost are as follows: The PCN-250-Fe₂Co (15 g) was synthesized using Fe₂Co clusters (11 g), H₄abtc (5.5 g), acetic acid (10 mL), and DMF (200 mL). The costs for Fe₂Co clusters and H₄abtc are CNY 0.568 and CNY 2.513 per gram, respectively. DMF, considering its recyclability, costs CNY 0.03 per mL, and acetic acid costs CNY 0.03 per gram. With a 90% yield, the total cost for producing PCN-250-Fe₂Co is about CNY 4.31 per gram. For the preparation of [Emim]BF₄@PCN-250-Fe₂Co, 9.71 g of [Emim]BF₄ at CNY 4.48 per gram is required. The total cost to prepare 24.71 g of the catalyst is CNY 108.15, making the cost approximately CNY 4.38 per gram.

Synthesis of NH₂-MIL-101(Fe). NH₂-MIL-101(Fe) were synthesized by solvothermal method⁵⁹. In brief, 2-aminoterephthalic acid (0.63 g, 2.50 mmol) and FeCl₃·6H₂O (0.23 g, 1.24 mmol) were dissolved in DMF (30 mL) for thermal reaction at 110 °C for 20 h, the final resulting brown solid was washed with DMF and ethanol, respectively.

Synthesis of HKUST-1. HKUST-1 was prepared based on a previously reported method⁶⁰. Briefly, copper nitrate hemipentahydrate (5 g) and benzene-1,3,5-tricarboxylic acid (2.5 g) were dissolved in DMF (125 mL). The solution kept at 75 °C for 24 h. The final resulting solid was washed with DMF and ethanol/water solution (1:2, v:v), respectively.

Synthesis of NH₂-UiO-66(Zr). NH₂-UiO-66 was synthesized by a previous reported method⁶¹. Briefly, 2-aminoterephthalic acid (0.14 g, 0.75 mmol), ZrCl₄ (0.13 g, 0.54 mmol), and concentrated HCl (1 mL) dissolved in DMF (15 mL) were being heated at 80 °C. Subsequently, the resultant suspension was centrifuged and washed anhydrous methanol.

Synthesis of NH₂-MIL-125(Ti). NH₂-MIL-125(Ti) prepared by a previous reported method⁶². Typically, titanium (IV) isopropoxide (0.177 mL, 0.6 mmol) and 2-aminoterephthalic acid (217 mg, 1.2 mmol) in mixture of DMF and CH₃OH (1:1, v:v) was heated at 150 °C for 15 h. A yellow solid powder was recovered by filtration, washed with DMF and CH₃OH.

Synthesis of ILs@PCN-250-Fe₂M. 3, 4, 5, 6, and 7 μL of 1-ethyl-3-methylimidazolium tetrafluoroborate ([Emim]BF₄), 1-ethyl-3-methylimidazolium acetate [Emim]Ac or 1-ethyl-3-methylimidazole bromide ([Emim]Br) were dispersed in 1 mL of anhydrous ethanol, respectively. Then, 10 mg of PCN-250-Fe₂M was added to the above system and stirred continuously with magnetic force for 24 h so that the ILs could enter the pores of PCN-250-Fe₂M. The composites was uniformly coated on glass sheet, and the obtained sample was dried under vacuum at 120 °C for 72 h to obtain a self-supporting ILs@PCN-250-Fe₂M film after anhydrous ethanol had been dried. The resulting samples can be directly used in photocatalytic reactions.

Synthesis of [Emim]BF₄@MOFs. The synthesis method is the same as that in 1.7. The following MOFs were used: NH₂-MIL-101(Fe), HKUST-1(Cu), NH₂-UiO-66 (Zr) or NH₂-MIL-125(Ti).

Characterizations. The characteristics of the materials were investigated by Fourier transform infrared (FT-IR) spectra (Avatar 370), power X-ray powder diffraction (PXRD) patterns (Panalytical X' Pert PRO). N₂ adsorption-desorption isotherms were determined by Micromeritics ASAP 2020 analyzer at 77 K. Scanning

electron microscopy (SEM) micrographs (Hitachi S-4800), the transmission electron microscopy (TEM) experiment (JEM-2100 electron microscope), diffuse reflectance UV-vis spectroscopy techniques (Shimadzu UV3600), and thermogravimetric analyses (TGA/SDTA851e), photoluminescence spectrum (PL) (Shimadzu RF-5301PC spectrofluorometer), X-ray photoelectron spectroscopy (XPS) techniques (Kratos-AXIS ULTRA DLD apparatus). The electrochemical impedance spectra (EIS), Mott-Schottky plot and photocurrent-time (I-T) profiles was recorded on the CHI660E electrochemical workstation with a standard three-electrode system with the photocatalyst-coated ITO as the working electrode, Pt plate as the counter electrode, and Ag/AgCl electrode as a reference electrode, A 300 W Xenon lamp with a 420 nm cut-off filter was used as the light source during the measurement. A 0.25 M Na₂SO₄ solution was used as the electrolyte. The as-synthesized samples (2 mg) were added into 1 mL ethanol and 10 μL Nafion mixed solution, and the working electrodes were prepared by dropping the suspension (200 μL) onto an ITO glass substrate electrode surface and dried at room temperature.

Photocatalytic CO₂ reduction experiments. The photocatalytic gas-solid CO₂ reduction activity test was carried out in the 80 mL gas-solid reactor, and gas products in the headspace of the reactor were measured using gas chromatography (GC-7920A, Aulight Co, China). Detailed procedure is as follows: 10 mg of sample was uniformly dispersed in 1 mL acetone solution, and then coated on a round glass sheet with a diameter of 4.5 cm, and then dried statically to obtain a self-supporting membrane on the glass sheet. Subsequently, 0.5 mL of deionized water was added into reactor. It was purged by high-purity CO₂ (or 15% CO₂ and 85% N₂) for 30 min to fully remove the air in the reactor, and then reactor was sealed under 1 atm CO₂ saturation. The reaction system was irradiated under 300 W Xe lamp (λ ≥ 420 nm). The gas samples were collected every 1 h, and the CO gas was detected by GC 7920 on-line gas chromatograph with FID and TID detector. The liquid products were collected and analyzed using ion chromatography and ¹H NMR spectroscopy. At the same time, the cooling circulating water temperature of the reactor is kept at 25 °C. The ¹³CO was analyzed by gas chromatography-mass spectrometry (7890A and 5975C, Agilent Technologies). In order to remove the ¹²CO₂ previously adsorbed by ILs, the tested samples were degassed in a vacuum drying oven at 120 °C, and the vacuum state was released with N₂ to prevent the rapid collection of ¹²CO₂ in the air by ILs. The analyzed method of ¹⁸O₂ was the same as that of ¹³CO.

Scaled-up experiments. Imitating industrial production, a large reactor composed of ten channels in series was built, with a total surface area of 1072 cm². In detail, we first prepare 1 g of catalyst and then divide it into ten equal parts. Each part of the catalyst (100 mg) is evenly dispersed in 5 mL acetone solution, and then coated on a rectangular glass sheet with 32 cm in length and 3 cm in width. After drying, it was placed in a large reactor, and then appropriate water is added to the gaps to seal the reactor. Subsequently, it was purged by high-purity CO₂ (or 15% CO₂ and 85% N₂) for 30 min to fully remove the air in the reactor, and then reactor was sealed under 1 atm CO₂ saturation. The reaction system was irradiated centrally by six 300 W Xe lamps (λ ≥ 420 nm) The gas samples were collected every 1 h, and the CO gas was detected by GC7920 on-line gas chromatograph with FID and TID detector. At the same time, the cooling circulating water temperature of the reactor is kept at 25 °C. We also put the reactor outdoors and conducted scaled-up experiments under sunlight for 60 h.

AQE determination. AQE for CO evolution was measured using 300 W xenon lamp with attenuation filter and band pass filter of 420, 450, 500, 550, 600, and 500 nm. Take an example, band pass filter is

450 nm. The formula for calculating the AQE is as follows:

$$\eta_{\text{co}}(\text{AQE}) = \frac{2 \times M \times N_A \times h \times c}{S \times P \times T \times \lambda}$$

Area (S) = $15.89 \times 10^{-4} \text{ m}^2$

Light power density (P) = 36.11 W/m^2 .

Time (T) = 3600 s

Wavelength (λ) = $450 \text{ nm} = 4.5 \times 10^{-7} \text{ m}$

Avogadro constant (N_A) = $6.02 \times 10^{23} \text{ mol}^{-1}$

Planck constant (h) = $6.626 \times 10^{-34} \text{ J}\cdot\text{s}$

speed of light (c) = $2.998 \times 10^8 \text{ m/s}$

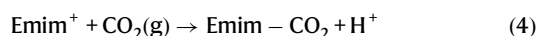
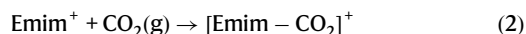
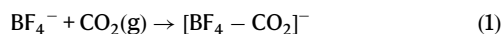
M is moles of product.

In one hour, the CO yields were determined to be $11.4498 \text{ } \mu\text{mol}$ (450 nm), by using 10 mg PCN-250-Fe₂Co as photocatalyst.

Calculation details and reaction mechanism

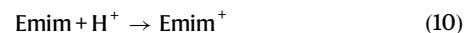
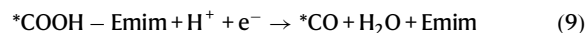
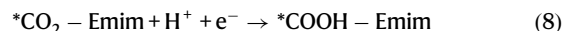
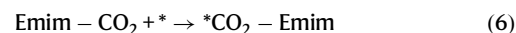
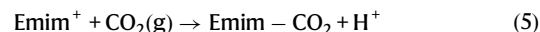
The crystal structure optimization and the density of state (DOS) calculations were performed using first-principle DFT as implemented in the software package VASP 5.4.4^{63,64}. The projector-augmented-wave (PAW) approach was used to describe the electron-ion interactions, and the Perdew–Burke–Ernzerhof (PBE) functional of the generalized gradient approximation (GGA) was used for the exchange–correlation interactions^{65–67}. The plane-wave energy cutoff was set to 400 eV, and the convergence of energy and force was $<10^{-5} \text{ eV}$ and $0.01 \text{ eV } \text{\AA}^{-1}$, respectively, for both lattice vectors and atomic positions. The Monkhorst-Pack k-point grid of $1 \times 1 \times 1$ was used to sample the Brillouin Zone for all calculations. All molecular geometries were optimized at the level of the B3LYP hybrid functional in the gas phase⁶⁸. For geometric optimization, the Lanl2dz basis set was employed for the Fe and Co, while the 6-31g was used for the other main-group elements, i.e. C, N, H, and O^{69,70}. The stationary frequency calculations at 298.15 K and 1 atm were performed at the same level for each of the optimized structures to examine any imaginary frequency, and obtain the thermal correction to Gibbs free energy through the corresponding vibrational modes. Then a higher precision setting including D3 dispersion correction developed by Grimme for weak interactions is used to perform single point calculations for obtaining a more accuracy self-consistent electronic energy⁷¹. The SDD basis set was employed for the Fe and Co, while the 6-311+g(d, p) was used for the other main-group elements^{72,73}. All of these calculations were performed by the Gaussian 09 program package⁷⁴. Free energy change of each elemental step was calculated by the following equation: $\Delta G = \Delta E + \Delta \text{ZPE} - T\Delta S$, where ΔE is the total self-consistent energy change, ΔZPE is the difference in zero-point energies (ZPE), and ΔS is the change of entropy. ZPE and entropies for intermediates were obtained from the vibrational frequency calculations. The free energy of $\text{H}^+ + \text{e}^-$ has been replaced by one-half of the chemical potential of the hydrogen molecule. The electrostatic potential analysis was performed by Multiwfn⁷⁵.

Four possible adsorption mechanisms of the CO₂ capture process on [Emim]BF₄ are as follows:



The host-guest synergistic mechanism of CO₂ reduction to CO in [Emim]BF₄@PCN-250-Fe₂Co is inferred as follows (* represents the

Co²⁺ sites in PCN-250-Fe₂Co):



Data availability

The data used in this study are presented in the text, Supplementary Information and Source data. The atomic coordinates of the optimized model for electronic structure calculations are provided as a separate Supplementary Data 1. Additional data and information are available from the corresponding author on request. Source data are provided with this paper.

References

- Jiang, Z. et al. Filling metal-organic framework mesopores with TiO₂ for CO₂ photoreduction. *Nature* **586**, 549 (2020).
- Burlacot, A. et al. Alternative photosynthesis pathways drive the algal CO₂-concentrating mechanism. *Nature* **605**, 366 (2022).
- Zu, X. et al. Reversible switching Cu^I/Cu^I single sites catalyze high-rate and selective CO₂ photoreduction. *Angew. Chem. Int. Ed.* **62**, e202215247 (2023).
- Shi, Y. et al. Simultaneous manipulation of bulk excitons and surface defects for ultrastable and highly selective CO₂ photoreduction. *Adv. Mater.* **33**, 2100143 (2021).
- Kosaka, F. et al. Direct and continuous conversion of flue gas CO₂ into green fuels using dual function materials in a circulating fluidized bed system. *Chem. Eng. J.* **450**, 138055 (2022).
- Vega, F. et al. Current status of CO₂ chemical absorption research applied to CCS: towards full deployment at industrial scale. *Appl. Energy* **260**, 114313 (2020).
- Lu, M. et al. Confining and highly dispersing single polyoxometalate clusters in covalent organic frameworks by covalent linkages for CO₂ photoreduction. *J. Am. Chem. Soc.* **144**, 1861 (2022).
- Wang, H.-N. et al. Recent progress and perspectives in heterogeneous photocatalytic CO₂ reduction through a solid-gas mode. *Coord. Chem. Rev.* **438**, 213906 (2021).
- Xu, C. et al. Adsorption mechanisms and regeneration heat analysis of a solid amine sorbent during CO₂ capture in wet flue gas. *Energy* **284**, 129379 (2023).
- Huang, N.-Y. et al. Electrostatic attraction-driven assembly of a metal-organic framework with a photosensitizer boosts photocatalytic CO₂ reduction to CO. *J. Am. Chem. Soc.* **143**, 17424 (2021).
- Chen, H. et al. Epitaxially grown silicon-based single-atom catalyst for visible-light-driven syngas production. *Nat. Commun.* **14**, 1719 (2023).
- Zou, W. et al. Metal-free photocatalytic CO₂ reduction to CH₄ and H₂O₂ under non-sacrificial ambient conditions. *Angew. Chem. Int. Ed.* **62**, e202313392 (2023).

13. Li, N. et al. Calix[4]arene-functionalized titanium-oxo compounds for perceiving differences in catalytic reactivity between mono- and multimetallic sites. *J. Am. Chem. Soc.* **145**, 16098 (2023).
14. Gao, S. et al. Ingenious artificial leaf based on covalent organic framework membranes for boosting CO₂ photoreduction. *J. Am. Chem. Soc.* **145**, 9520 (2023).
15. Huang, H. et al. Triphase photocatalytic CO₂ reduction over silver-decorated titanium oxide at a gas-water boundary. *Angew. Chem. Int. Ed. Engl.* **61**, e202200802 (2022).
16. Si, S. et al. Low-coordination single Au atoms on ultrathin ZnIn₂S₄ nanosheets for selective photocatalytic CO₂ reduction towards CH₄. *Angew. Chem. Int. Ed.* **61**, e202209446 (2022).
17. Rao, H. et al. Visible-light-driven methane formation from CO₂ with a molecular iron catalyst. *Nature* **548**, 74 (2017).
18. Lyu, W. et al. Modulating the reaction configuration by breaking the structural symmetry of active sites for efficient photocatalytic reduction of low-concentration CO₂. *Angew. Chem. Int. Ed.* **62**, e202310733 (2023).
19. Qian, G. et al. Efficient photoreduction of diluted CO₂ to tunable syngas by Ni-Co dual sites through d-band center manipulation. *Angew. Chem. Int. Ed.* **61**, e202210576 (2022).
20. Han, B. et al. Nickel metal-organic framework monolayers for photoreduction of diluted CO₂: metal-node-dependent activity and selectivity. *Angew. Chem. Int. Ed.* **57**, 16811 (2018).
21. Lei, K. et al. A metal-free donor-acceptor covalent organic framework photocatalyst for visible-light-driven reduction of CO₂ with H₂O. *ChemSusChem* **13**, 1725 (2020).
22. Choi, C. et al. Synergizing electron and heat flows in photocatalyst for direct conversion of captured CO₂. *Angew. Chem. Int. Ed.* **62**, e202302152 (2023).
23. Ran, J. et al. Cocatalysts in semiconductor-based photocatalytic CO₂ reduction: achievements, challenges, and opportunities. *Adv. Mater.* **30**, 1704649 (2018).
24. Lv, H. et al. Boosting photocatalytic reduction of the diluted CO₂ over covalent organic framework. *Chem. Eng. J.* **451**, 138745 (2023).
25. Yang, Y. et al. Integrating enrichment, reduction, and oxidation sites in one system for artificial photosynthetic diluted CO₂ reduction. *Adv. Mater.* **35**, 2304170 (2023).
26. Huang, N.-Y. et al. Coupling ruthenium bipyridyl and cobalt imidazolate units in a metal-organic framework for an efficient photosynthetic overall reaction in diluted CO₂. *J. Am. Chem. Soc.* **144**, 8676 (2022).
27. Yang, W. et al. Tailoring crystal facets of metal-organic layers to enhance photocatalytic activity for CO₂ reduction. *Angew. Chem. Int. Ed.* **60**, 409 (2021).
28. Yue, X. et al. Highly strained Bi-MOF on bismuth oxyhalide support with tailored intermediate adsorption/desorption capability for robust CO₂ photoreduction. *Angew. Chem. Int. Ed.* **61**, e202208414 (2022).
29. Dong, Y.-L. et al. Immobilizing Isatin-Schiff base complexes in NH₂-UiO-66 for highly photocatalytic CO₂ reduction. *ACS Catal.* **13**, 2547 (2023).
30. Huang, Z.-W. et al. Thermally induced orderly alignment of porphyrin photoactive motifs in metal-organic frameworks for boosting photocatalytic CO₂ reduction. *J. Am. Chem. Soc.* **145**, 18148 (2023).
31. Chen, H.-Y. et al. Integration of Ru(II)-bipyridyl and Zinc(II)-porphyrin moieties in a metal-organic framework for efficient overall CO₂ photoreduction. *Acta Phys. -Chim. Sin.* **40**, 2306046 (2024).
32. Wu, K. et al. Linker engineering for reactive oxygen species generation efficiency in ultra-stable nickel-based metal-organic frameworks. *J. Am. Chem. Soc.* **145**, 18931 (2023).
33. Karmakar, S. et al. Confining charge-transfer complex in a metal-organic framework for photocatalytic CO₂ reduction in water. *Nat. Commun.* **14**, 4508 (2023).
34. Zhao, C. et al. Molecular compartments created in metal-organic frameworks for efficient visible-light-driven CO₂ Overall Conversion. *J. Am. Chem. Soc.* **144**, 23560 (2022).
35. Zheng, H.-L. et al. Multilevel-regulated metal-organic framework platform integrating pore space partition and open-metal sites for enhanced CO₂ photoreduction to CO with nearly 100% selectivity. *J. Am. Chem. Soc.* **145**, 27728 (2023).
36. Cai, P. et al. Precise spatial-designed metal-organic-framework nanosheets for efficient energy transfer and photocatalysis. *Angew. Chem. Int. Ed.* **60**, 27258 (2021).
37. Fang, Z.-B. et al. Boosting interfacial charge-transfer kinetics for efficient overall CO₂ photoreduction via rational design of coordination spheres on metal-organic frameworks. *J. Am. Chem. Soc.* **142**, 12515 (2020).
38. Dong, L.-Z. et al. Stable heterometallic cluster-based organic framework catalysts for artificial photosynthesis. *Angew. Chem. Int. Ed.* **59**, 2659 (2020).
39. Wang, W. et al. Metal-organic framework-based materials as platforms for energy applications. *Chem.* **10**, 86 (2024).
40. Sun, K. et al. Metal-organic frameworks for photocatalytic water splitting and CO₂ reduction. *Angew. Chem. Int. Ed.* **64**, e202217565 (2023).
41. Stanley, P. M. et al. Merging molecular catalysts and metal-organic frameworks for photocatalytic fuel production. *Nature Chemistry* **14**, 1342 (2022).
42. Suo, X. et al. CO₂ chemisorption behavior in conjugated carbanion-derived ionic liquids via carboxylic acid formation. *J. Am. Chem. Soc.* **144**, 21658 (2022).
43. Liu, Y. et al. Improving CO₂ photoconversion with ionic liquid and Co single atoms. *Nat. Commun.* **14**, 1457 (2023).
44. He, X. et al. EMmim][NTf₂—a novel ionic liquid (IL) in catalytic CO₂ capture and its applications. *Adv. Sci.* **10**, 2205352 (2023).
45. Wang, G. et al. Engineering a copper single-atom electron bridge to achieve efficient photocatalytic CO₂ conversion. *Angew. Chem. Int. Ed. Engl.* **62**, e202218460 (2023).
46. Xue, W.-L. et al. Reticular chemistry for ionic liquid-functionalized metal-organic frameworks with high selectivity for CO₂. *ACS Sustain. Chem. Eng.* **8**, 18558 (2020).
47. Feng, D. et al. Kinetically tuned dimensional augmentation as a versatile synthetic route towards robust metal-organic frameworks. *Nat. Commun.* **5**, 5723 (2014).
48. An, J.-R. et al. Efficient visible-light photoreduction of CO₂ to CH₄ over an Fe-based metal-organic framework (PCN-250-Fe₃) in a solid-gas mode. *ACS Appl. Energy Mater.* **5**, 2384 (2022).
49. Shi, Y. et al. An anti-freezing hydrogel electrolyte for flexible zinc-ion batteries operating at -70 °C. *Adv. Funct. Mater.* **33**, 2214546 (2023).
50. Yan, W. et al. Anion modulation of Ag-imidazole cuboctahedral cage microenvironments for efficient electrocatalytic CO₂ reduction. *Angew. Chem. Int. Ed.* **63**, e202406564 (2024).
51. Sun, W. et al. Electrochemistry and electrocatalysis of hemoglobin on multi-walled carbon nanotubes modified carbon ionic liquid electrode with hydrophilic EMIMBF₄ as modifier. *Electrochim. Acta* **54**, 4141 (2009).
52. Xiao, Z. et al. Unusual phase separation and rheological behavior of poly(ethylene oxide)/ionic liquid mixtures with specific interactions. *Soft Matter* **12**, 7613 (2016).
53. Katsyuba, S. A. et al. Molecular structure, vibrational spectra, and hydrogen bonding of the ionic liquid 1-ethyl-3-methyl-1H-imidazolium tetrafluoroborate. *Helv. Chim. Acta* **87**, 2556 (2004).
54. Ishikawa, A. et al. Oxysulfide Sm₂Ti₂S₂O₅ as a stable photocatalyst for water oxidation and reduction under visible light irradiation ($\lambda \leq 650$ nm). *J. Am. Chem. Soc.* **124**, 13547 (2002).

55. Zhou, J. et al. Linking oxidative and reductive clusters to prepare crystalline porous catalysts for photocatalytic CO₂ reduction with H₂O. *Nat. Commun.* **13**, 4681 (2022).
56. Yang, X. et al. Oxygen vacancies induced special CO₂ adsorption modes on Bi₂MoO₆ for highly selective conversion to CH₄. *Appl. Catal. B Environ.* **259**, 118088 (2019).
57. Guo, F. et al. Designing heteroatom-codoped iron metal-organic framework for promotional photoreduction of carbon dioxide to ethylene. *Angew. Chem. Int. Ed.* **62**, e202216232 (2023).
58. Peng, L. et al. Using predefined M₃(μ₃-O) clusters as building blocks for an isostructural series of metal-organic frameworks. *ACS Appl. Mat. Interfaces* **9**, 23957 (2017).
59. Liu, M. et al. Cerium-doped MIL-101-NH₂(Fe) as superior adsorbent for simultaneous capture of phosphate and As(V) from Yangzonghai coastal spring water. *J. Hazard. Mater.* **423**, 126981 (2022).
60. Yan, X. et al. Extremely enhanced CO₂ uptake by HKUST-1 metal-organic framework via a simple chemical treatment. *Micropor. Mesopor. Mat.* **183**, 69 (2014).
61. Bi, Q.-Q. et al. Selective photocatalytic CO₂ reduction in water by electrostatic assembly of CdS nanocrystals with a dinuclear cobalt catalyst. *ACS Catal.* **8**, 11815 (2018).
62. Khaletskaia, K. et al. Fabrication of gold/titania photocatalyst for CO₂ reduction based on pyrolytic conversion of the metal-organic framework NH₂-MIL-125(Ti) loaded with gold nanoparticles. *Chem. Mater.* **27**, 7248 (2015).
63. Kresse, G. et al. Ab initio molecular dynamics for open-shell transition metals. *Phys. Rev. B* **48**, 13115 (1993).
64. Kresse, G. et al. Efficient iterative schemes for ab initio total-energy calculations using a plane-wave basis set. *Phys. Rev. B* **54**, 11169 (1996).
65. Kresse, G. et al. Efficiency of ab-initio total energy calculations for metals and semiconductors using a plane-wave basis set. *Comput. Mater. Sci.* **6**, 15 (1996).
66. Blöchl, P. E. Projector augmented-wave method. *Phys. Rev. B* **50**, 17953 (1994).
67. Perdew, J. P. et al. Generalized gradient approximation made simple. *Phys. Rev. Lett.* **77**, 3865 (1996).
68. Becke, A. D. Density-functional thermochemistry. III. The role of exact exchange. *J. Chem. Phys.* **98**, 5648 (1993).
69. Hay, P. J. et al. Ab initio effective core potentials for molecular calculations. Potentials for K to Au including the outermost core orbitals. *J. Chem. Phys.* **82**, 299 (1985).
70. Ditchfield, R. et al. Self-consistent molecular-orbital methods. IX. An extended Gaussian-type basis for molecular-orbital studies of organic molecules. *J. Chem. Phys.* **54**, 724 (2003).
71. Grimme, S. et al. A consistent and accurate ab initio parametrization of density functional dispersion correction (DFT-D) for the 94 elements H-Pu. *J. Chem. Phys.* **132**, 154104 (2010).
72. Krishnan, R. et al. Self-consistent molecular orbital methods. XX. A basis set for correlated wave functions. *J. Chem. Phys.* **72**, 650 (2008).
73. Neese, F. et al. Revisiting the atomic natural orbital approach for basis sets: robust systematic basis sets for explicitly correlated and conventional correlated AB initio methods? *J. Chem. Theory Comput.* **7**, 33 (2011).
74. Frisch, G. S. M. T. et al. *Gaussian 09, revision a. 02* (Gaussian, Inc., 2009).
75. Lu, T. et al. Multiwfn: a multifunctional wavefunction analyzer. *J. Comput. Chem.* **33**, 580 (2012).

Acknowledgements

F.Z. acknowledges the financial supports from National Natural Science Foundation of China (No. 22178077), Postdoctoral Scientific Research

Start-up Project in Heilongjiang Province (No. LBH-Q19111) and Shandong Provincial Natural Science Foundation (No. ZR2022MB126); L.S. acknowledges Youth Program of the National Natural Science Foundation of China (No. 22308072), Heilongjiang Postdoctoral Foundation (No. LBH-Z22191) and China Postdoctoral Science Foundation Funded Project (No. 2023M730887); Y.W. is thankful for Fundamental Research Foundation for Universities of Heilongjiang Province (No. 2020-KYYWF-0337), Young Talents of Basic Research in Universities of Heilongjiang Province (No. YQJH2023267) and Heilongjiang Province ecological environmental protection research project (No. HST2023ST004). G.Z. is thankful for Heilongjiang Provincial Natural Science Foundation of China (No. ZD2023B001).

Author contributions

F.Z. and Y.L. conceived and supervised the entire project. Y.W. and J.W. prepared the materials and carried out the photocatalytic activity tests and materials characterizations. Y. W. carried out the DFT calculations. J.W., X.C., and H.T. did TEM, FTIR, XPS analysis. G.Z., Y.J., L.S., and L.D. discussed the reaction mechanism. Y.W. and J.W. wrote the manuscript and data analysis. All authors contributed to discussion and revisions.

Competing interests

The authors declare no competing interests.

Additional information

Supplementary information The online version contains supplementary material available at <https://doi.org/10.1038/s41467-024-53066-y>.

Correspondence and requests for materials should be addressed to Feng-Ming Zhang or Ya-Qian Lan.

Peer review information *Nature Communications* thanks Shigeyuki Masaoka, who co-reviewed with Marc YauPei-Qin Liao; and the other, anonymous, reviewer(s) for their contribution to the peer review of this work. A peer review file is available.

Reprints and permissions information is available at <http://www.nature.com/reprints>

Publisher's note Springer Nature remains neutral with regard to jurisdictional claims in published maps and institutional affiliations.

Open Access This article is licensed under a Creative Commons Attribution-NonCommercial-NoDerivatives 4.0 International License, which permits any non-commercial use, sharing, distribution and reproduction in any medium or format, as long as you give appropriate credit to the original author(s) and the source, provide a link to the Creative Commons licence, and indicate if you modified the licensed material. You do not have permission under this licence to share adapted material derived from this article or parts of it. The images or other third party material in this article are included in the article's Creative Commons licence, unless indicated otherwise in a credit line to the material. If material is not included in the article's Creative Commons licence and your intended use is not permitted by statutory regulation or exceeds the permitted use, you will need to obtain permission directly from the copyright holder. To view a copy of this licence, visit <http://creativecommons.org/licenses/by-nc-nd/4.0/>.

© The Author(s) 2024